

AT Loss: Advanced Torrential Loss Function for Precipitation Forecasting

Jaeho Choi,^{1,2,*} Hyeri Kim,^{3,4,†} Kwang-Ho Kim,^{2,‡} and Jaesung Lee^{1,5,§}

¹*AI/ML Innovation Research Center, Chung-Ang University, Seoul 06974, Republic of Korea*

²*Weather Radar Center, Korea Meteorological Administration, Seoul 07062, Republic of Korea*

³*Advanced Radar Research Center, University of Oklahoma, Norman, OK 73019, USA*

⁴*School of Meteorology, University of Oklahoma, Norman, OK 73072, USA*

⁵*Department of Artificial Intelligence, Chung-Ang University, Seoul 06974, Republic of Korea*

(Dated: September 3, 2025)

Accurate precipitation forecasting is becoming increasingly important in the context of climate change. In response, machine learning-based approaches have recently gained attention as an emerging alternative to traditional methods such as numerical weather prediction and climate models. Nonetheless, many recent approaches still rely on off-the-shelf loss functions, and even the more advanced ones merely involve optimization processes based on the critical success index (CSI). The problem, however, is that CSI may become ineffective during extended dry periods when precipitation remains below the threshold, rendering it less than ideal as a criterion for optimization. To address this limitation, we introduce a simple penalty expression and reinterpret it as a quadratic unconstrained binary optimization (QUBO) formulation. Ultimately, the resulting QUBO formulation is relaxed into a differentiable advanced torrential (AT) loss function through an approximation process. The proposed AT loss demonstrates its superiority through the Lipschitz constant, forecast performance evaluations, consistency experiments, and ablation studies with the operational model.

Introduction.—Climate change has altered weather patterns, giving rise to meteorological phenomena not previously observed in certain regions [1, 2]. Extreme weather events are being recorded with increasing frequency worldwide, and the adverse impacts have intensified, especially from localized torrential rainfall and extended dry periods [3–5]. These events, by inducing frequent outliers, underscore the need to maintain reliable precipitation forecasting performance under such conditions. In this context, the critical success index (CSI) has come to be regarded as the metric most often considered first in evaluating precipitation forecasting [6, 7]. In practice, recently emerging machine learning (ML)-based approaches use CSI as the criterion to optimize forecast quality. They achieve this either by employing complex architectures or by simply incorporating CSI as a constraint term in objective functions with multiple loss functions [8–10]. Nevertheless, the primary loss functions, which remain the centerpiece of optimization, still rely on off-the-shelf designs, and even the suitability of CSI as a criterion for optimization remains debated.

In this Letter, we propose an advanced torrential (AT) loss function for broad use in ML-based precipitation forecasting, following the identification of the mathematical limitations of the CSI as an optimization criterion and addressing them through a binary penalty. The binary penalty is computed for each grid cell, equivalent to a pixel in the image domain, and the aggregated penalty forms the foundation of the AT loss. Furthermore, the overall penalty is expressed in the quadratic unconstrained binary optimization (QUBO) formulation and approximated as a differentiable surrogate using the binary Gumbel-Softmax, forming the AT loss that converges toward minimizing the penalty [11, 12]. The AT loss is validated in three key aspects. The first aspect

is training stability, ensured by a low Lipschitz constant in the early stage of training. The second aspect is forecast performance, evaluated by how accurately precipitation greater than or equal to the operational threshold is simulated across lead times, with outperformance confirmed via various forecasting metrics. In particular, forecast performance is validated via a convolutional long short-term memory (ConvLSTM) encoder-decoder model, which serves as a widely used benchmark in precipitation forecasting [13]. The third aspect is performance consistency under outliers, which can be induced by extreme weather events, with its superiority confirmed through comparisons with commonly used pixel-wise loss functions. From a practical standpoint, the effectiveness of the AT loss is further demonstrated through ablation studies using the paired complementary temporal cycle-consistent adversarial networks (PCT-CycleGAN) [10].

Characteristics of CSI.—Given real precipitation data $X^t = (x_i^t)_{i=1}^n$ from n grid cells at time step t , the ML-based forecasting model is trained to generate forecast data $Y^{t+1} = (y_i^{t+1})_{i=1}^n$ that closely approximates the ground-truth X^{t+1} . In particular, recent advanced models aim to make the CSI of Y^{t+1} as close to 1 as possible through iterative training [8, 10]. This metric, denoted as $\text{CSI}(Y^{t+1})$ is computed as

$$\text{CSI}(Y^{t+1}) = \frac{\sum_{i=1}^n (f(x_i^{t+1}) \wedge f(y_i^{t+1}))}{\sum_{i=1}^n (f(x_i^{t+1}) \vee f(y_i^{t+1}))},$$

$$\text{where } f(k) = \begin{cases} 1, & \text{if } k \geq \theta, \\ 0, & \text{otherwise.} \end{cases} \quad (1)$$

Here, $f(k)$ is a step function and $\theta \in \mathbb{R}_{\geq 0}$ denotes the threshold. According to Eq. (1), when all values fall below the threshold, the denominator of $\text{CSI}(Y^{t+1})$ be-

TABLE I. Binary penalty for four distinct cases.

Case	$f(x_i^{t+1})$	$f(y_i^{t+1})$	Forecast	Penalty
1	0	0	True	0
2	0	1	False	1
3	1	0	False	1
4	1	1	True	0

comes 0, making it unreliable during extended dry periods with negligible or no precipitation. Furthermore, the numerator of $\text{CSI}(Y^{t+1})$ excludes any grid cell i where both $f(x_i^{t+1})$ and $f(y_i^{t+1})$ are 0, even though such cases represent correct forecasts. In addition to these characteristics, the presence of $f(k)$ makes $\text{CSI}(Y^{t+1})$ non-differentiable and therefore cannot be directly optimized with gradient descent [14, 15]. Thus, the CSI is suboptimal as a training criterion. Nonetheless, since the CSI is effective for evaluating precipitation forecasts, an advanced optimization criterion that builds on its strengths while addressing its limitations is required.

Binary Penalty.—Based on Eq. (1), the forecast at grid cell i for time step $t + 1$ can be divided into four distinct cases, as shown in Table I. In case 1, both the real value x_i^{t+1} and the generated forecast value y_i^{t+1} are below the threshold θ , meaning that $f(x_i^{t+1}) = f(y_i^{t+1}) = 0$. In this case, the forecast outcome at grid cell i cannot affect $\text{CSI}(Y^{t+1})$. Since this point gives rise to the limitations of CSI, a binary penalty is introduced as a straightforward solution. The penalty is applied only to incorrect forecasts that are considered false. Thus, cases 1 and 4, where $f(x_i^{t+1}) = f(y_i^{t+1})$, are true forecasts with no penalty, while cases 2 and 3, where $f(x_i^{t+1}) \neq f(y_i^{t+1})$, are false forecasts with a penalty of 1. Ultimately, the binary penalty P_i^{t+1} at grid cell i is defined as

$$P_i^{t+1} = f(x_i^{t+1}) + f(y_i^{t+1}) - 2f(x_i^{t+1})f(y_i^{t+1}). \quad (2)$$

The overall penalty P^{t+1} , which is the sum of P_i^{t+1} , simplifies to

$$P^{t+1} = \sum_{i=1}^n (f(x_i^{t+1}) - f(y_i^{t+1}))^2. \quad (3)$$

Since improving forecast performance requires minimizing Eq. (3), this expression naturally serves as the objective function of the QUBO formulation and a potential criterion for optimizing ML-based approaches [16–18].

Approximation.—The most suitable approach to using Eq. (3) in optimizing ML-based forecasting models is to let it serve as the foundation of the loss function. This is achieved by approximating only $f(y_i^{t+1})$, since $f(x_i^{t+1})$ is fixed by the constant x_i^{t+1} . To this end, $f(y_i^{t+1})$ can be approximated via binary Gumbel-Softmax, a differentiable relaxation of Bernoulli sampling [19, 20]. This method is stable and can sharply discriminate the threshold, allowing accurate identification of the presence or absence of precipitation when integrated with the QUBO

formulation. In this context, the logits for 1 and 0 are represented as $l_1 = y_i^{t+1} - \theta$ and $l_0 = -l_1$, respectively, depending on the threshold θ . The resulting approximation $\tilde{f}(y_i^{t+1})$ is defined as

$$\begin{aligned} \tilde{f}(y_i^{t+1}) &= \frac{1}{1 + \exp\left(-\frac{1}{\tau}(l_1 - l_0 + g_1 - g_0)\right)} \\ &= \sigma\left(\frac{1}{\tau}(2y_i^{t+1} - 2\theta + z)\right), \end{aligned} \quad (4)$$

where $g_0, g_1 \sim \text{Gumbel}(0, 1)$ and $z \sim \text{Logistic}(0, 1)$. Note that $\tau > 0$ is the temperature parameter and $\sigma(\cdot)$ is the sigmoid function.

AT Loss.—According to Eqs. (3)–(4), the mean of the approximation of P^{t+1} can be used as the loss function. Therefore, the proposed AT loss between the ground-truth X^{t+1} and the forecasts Y^{t+1} is defined as

$$\begin{aligned} \mathcal{L}(X^{t+1}, Y^{t+1}; \tau, \theta, z) &= \frac{1}{n} \sum_{i=1}^n \mathcal{L}_i \\ &= \frac{1}{n} \sum_{i=1}^n \left(f(x_i^{t+1}) - \sigma\left(\frac{1}{\tau}(2y_i^{t+1} - 2\theta + z)\right) \right)^2, \end{aligned} \quad (5)$$

where \mathcal{L}_i is the individual loss for grid cell i . Here, z is obtained through inverse transform sampling as $\ln u - \ln(1 - u)$, where $u \sim \text{Uniform}(0, 1)$. In the actual implementation, $\tau \in (0, 1]$ is gradually decayed across training epochs, and the perturbation is constrained by $|z| \ll 1$. This strategy helps ensure stable optimization while leveraging a proven annealing-based hyperparameter control technique [20, 21]. Another point to note is that, as the AT loss already involves $\sigma(\cdot)$, the activation function at the output layer should be omitted, or the pre-activation values should be used, to avoid information loss from redundant non-linear transformations.

Training Stability.—According to Eq. (5), differentiating \mathcal{L}_i with respect to y_i^{t+1} yields

$$\begin{aligned} \frac{\partial \mathcal{L}_i}{\partial y_i^{t+1}} &= -\frac{4}{\tau} (f(x_i^{t+1}) - \zeta) \zeta (1 - \zeta), \\ \text{where } \zeta &= \sigma\left(\frac{1}{\tau}(2y_i^{t+1} - 2\theta + z)\right). \end{aligned} \quad (6)$$

Since $f(x_i^{t+1}) \in \{0, 1\}$, Eq. (6) simplifies as

$$\frac{\partial \mathcal{L}_i}{\partial y_i^{t+1}} = \begin{cases} -\frac{4}{\tau} (\zeta^3 - \zeta^2), & \text{if } f(x_i^{t+1}) = 0, \\ -\frac{4}{\tau} (\zeta^3 - 2\zeta^2 + \zeta), & \text{otherwise.} \end{cases} \quad (7)$$

Differentiating Eq. (7) with respect to ζ simplifies to

$$\frac{\partial}{\partial \zeta} \left(\frac{\partial \mathcal{L}_i}{\partial y_i^{t+1}} \right) = \begin{cases} -\frac{4}{\tau} \zeta (3\zeta - 2), & \text{if } f(x_i^{t+1}) = 0, \\ -\frac{4}{\tau} (\zeta - 1) (3\zeta - 1), & \text{otherwise.} \end{cases} \quad (8)$$

TABLE II. Forecast performance comparisons.

Loss	CSI	HSS	POD	FAR
20-minute lead time				
AT	0.6015	0.7478	0.7173	0.2117
MAE	0.5618	0.7165	0.6658	0.2174
MSE	0.5055	0.6673	0.7538	0.3945
Huber	0.4375	0.6047	0.5431	0.3077
Charbonnier	0.5702	0.7231	0.7146	0.2616
40-minute lead time				
AT	0.4980	0.6606	0.6093	0.2684
MAE	0.4590	0.6253	0.5626	0.2865
MSE	0.4134	0.5792	0.7082	0.5018
Huber	0.3746	0.5402	0.4974	0.3973
Charbonnier	0.4612	0.6273	0.5895	0.3206
60-minute lead time				
AT	0.4172	0.5838	0.5176	0.3174
MAE	0.3830	0.5495	0.4759	0.3377
MSE	0.3507	0.5124	0.6664	0.5747
Huber	0.3386	0.5000	0.5140	0.5020
Charbonnier	0.3798	0.5459	0.4908	0.3732

Thus, the extremum of Eq. (7) is attained when $\zeta = \frac{2}{3}$ for $f(x_i^{t+1}) = 0$, and when $\zeta = \frac{1}{3}$ for $f(x_i^{t+1}) = 1$. Substituting the value of ζ for each case, the Lipschitz constant of \mathcal{L}_i is obtained as $\frac{16}{27\tau} \approx 0.5926\tau^{-1}$. In practice, the fact that the Lipschitz constant remains below 1 in the interval $\tau \in [0.6, 1]$, where most of the optimization takes place, guarantees the stability of the training process.

Data and Settings.—The AT loss was evaluated based on training and test datasets derived from composite hybrid surface rainfall (HSR) data of the Korea Meteorological Administration (KMA) used in official weather forecasting [10, 22]. Each instance of HSR data represents the precipitation intensity over a $1024 \text{ km} \times 1024 \text{ km}$ domain covering the entire Republic of Korea. The training dataset was constructed from HSR data spanning 2022 to 2023, whereas the test dataset was constituted from data collected between January and August 2024, together with data obtained in July 2025. Both datasets were specified at spatial and temporal resolutions of 4 km and 10 minutes, respectively. In particular, to preserve temporal causality, the datasets were organized using a sliding-window approach, where each window consisted of six consecutive time steps [23, 24]. The datasets were normalized to the range $[-1, 1]$. Details of hyperparameter settings are provided in the End Matter.

Baselines.—The AT loss was compared with various pixel-wise loss functions. The mean absolute error (MAE) and mean squared error (MSE) losses, widely used in the field, were adopted as baselines [25]. Additionally, the Huber and Charbonnier losses, which combine the advantages of the previous two losses while providing robustness, were also included as baselines [26–28].

Forecast Evaluations with Benchmark.—Comparative experiments were conducted on the AT loss using the ConvLSTM encoder-decoder model, a benchmark in ML-

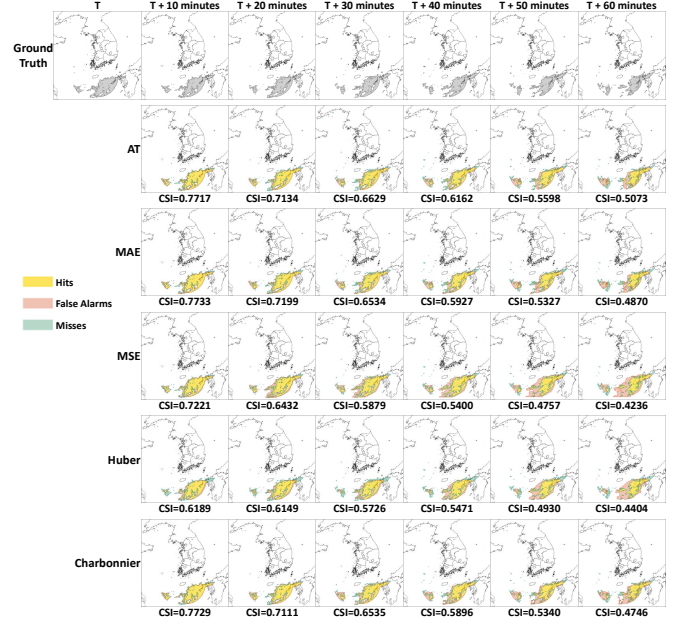


FIG. 1. A case of precipitation forecast comparisons from time T (2024-06-26 01:50:00 UTC).

based operational precipitation forecasting systems [13]. The evaluation adopted four recommended metrics for weather forecasting verification: CSI, Heidke skill score (HSS), probability of detection (POD), and false alarm ratio (FAR) [29, 30]. Better forecasting performance is indicated when FAR approaches 0, while the other metrics are better when closer to 1.

According to Table II, the AT loss achieved the best CSI, HSS, and FAR across all lead times of 20, 40, and 60 minutes, outperforming the other baselines. Although the MSE loss showed the highest POD, this came with the highest FAR. Since effective forecasts require both high POD and low FAR, the AT loss provided the best overall balance, demonstrating superior performance.

To enable a more intuitive comparison, Fig. 1 illustrates a case of 1-hour forecasts at 01:50:00 UTC on June 26, 2024. The highlighted areas represent regions with precipitation intensity greater than or equal to 2 mm/h. In this case, the AT loss produced the best forecasts beginning from the 30-minute lead time. In particular, it most accurately simulated the eastward-moving precipitation echoes. As a supplement, an additional case is presented in Fig. 3 of the End Matter.

Consistency Experiments under Outliers.—The performance consistency of the AT loss under outliers was verified through comparative experiments with baselines. To use only the intended outliers in the experiments, the interquartile range of the original data was first calculated, and Tukey’s method was applied to identify the existing outliers within the range [31, 32]. The identified outliers were replaced with the mean precipitation intensity of

TABLE III. Performance differences under outliers.

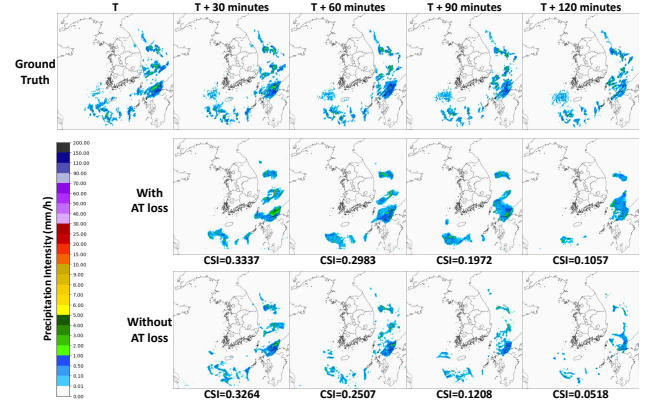
Loss	MAE	PSNR
Salt-and-pepper noise		
AT	2.4251	33.8598
MAE	4.0917	33.4847
MSE	8.9409	27.4833
Huber	4.2883	33.4819
Charbonnier	4.5570	33.2172
Random-valued impulse noise		
AT	2.9976	34.0679
MAE	5.3458	32.2673
MSE	11.1006	25.4866
Huber	4.9959	33.0321
Charbonnier	5.4007	32.0984

neighboring grid cells. Then, this refined data was used to train a convolutional neural network (CNN) for 1-step forecasting in two tracks, clean and dirty, for each loss function, with architectural details provided in the End Matter. The clean track used the refined data as is for training. In the dirty track, intentional noise was injected as the refined data was fed into the CNN. Specifically, 10 to 30 percent of the refined data was randomly corrupted with salt-and-pepper noise and random-valued impulse noise [33, 34]. After training, forecasts from both tracks were compared in terms of MAE and peak signal-to-noise ratio (PSNR) [35, 36]. The lower the MAE and the higher the PSNR between the forecasts from the clean and dirty tracks, the more consistent the performance of the loss function is, regardless of contamination.

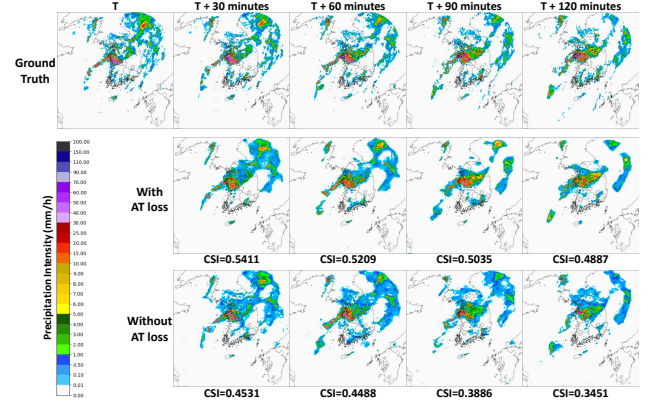
As presented in Table III, the AT loss achieved the lowest MAE and the highest PSNR across both noise types, clearly outperforming the baselines. It is particularly encouraging that the performance gap was more pronounced under random-valued impulse noise, which better reflects realistic scenarios. These results suggest that the AT loss enables stable training, allowing forecasting models to maintain consistent performance in the presence of outliers induced by extreme weather events.

Ablation Studies.—To evaluate the contribution of AT loss to forecast performance in operational practice, ablation studies were conducted using the 2025 version of the PCT-CycleGAN [10]. This version, adapted from the initial model, replaced shot-to-shot processing with a sequence-to-sequence framework and upgraded the torrential loss into AT loss. All other experimental conditions remained identical, with the only difference being the presence or absence of AT loss. For reproducibility, the ablation studies utilized the KMA color map and applied an operational CSI threshold of 0.5 mm/h.

Fig. 2a presents 2-hour forecasts of a light precipitation case. The initial time T is 00:00:00 UTC on January 10, 2024. In this case, the threshold for AT loss was set to 0.5 mm/h, with a focus on light precipitation. For all lead times, the model with AT loss outperformed the



(a) Case forecast initialized at time T (2024-01-10 00:00:00 UTC).



(b) Case forecast initialized at time T (2025-07-16 15:00:00 UTC).

FIG. 2. Forecasts with and without advanced torrential (AT) loss in ablation studies on light and heavy precipitation cases.

one without it in terms of the CSI metric, and the gap between the two grew over time. In the final lead time, the model with AT loss achieved more than twice the CSI of the model without it. This suggests a positive effect on improving forecasting performance for light precipitation, which is more challenging than typical cases.

Fig. 2b shows the 2-hour forecasts for a heavy precipitation case starting at 15:00:00 UTC on July 16, 2025. This case represents an exceptionally intense regional precipitation event. The model with AT loss outperformed the one without it across all lead times, and at the last lead time, it achieved approximately 42 percent higher CSI. From a qualitative perspective, meteorologists at the KMA judged that the model incorporating AT loss provided a more accurate simulation of heavy precipitation areas than the model without it.

Since the primary objective of AT loss is not to determine the exact value of each grid cell but to identify whether it is greater than or equal to the threshold, it is most effective when combined with other loss functions that guide the model toward accurate values. Therefore, when applying AT loss in operational models, it is

important to seek a balance with these complementary loss functions. In other words, empirical strategies aimed at achieving optimal forecasts, including adjusting the weights across loss functions, employing staged training, and fine-tuning, are essential.

Conclusion.—In this study, we introduced a grid cell-level binary penalty to overcome the limitations of CSI. On this basis, we proposed the AT loss, formulated with QUBO and the binary Gumbel-Softmax, to advance ML-based forecasting. The AT loss was designed to ensure stable convergence in early training and sharp threshold discrimination in later stages. Experiments showed that AT loss delivered the best forecast performance and was consistent under outliers, with its effectiveness further supported by ablation studies in operational settings. Nevertheless, broader validation across operational models in different countries remains a common challenge for the atmospheric physics and meteorology communities.

Acknowledgments.—The authors thank Yura Kim and Seongmook Kim for insightful discussions. This work was supported by the Institute of Information & Communications Technology Planning & Evaluation (IITP) grant funded by the Korea government (MSIT) [RS-2021-II211341, Artificial Intelligence Graduate School Program (Chung-Ang University)], and the Development of Integrated Application Technology for Korea Weather Radar project funded by the Weather Radar Center, Korea Meteorological Administration [KMA2021-03122, Development of Radar Based Severe Weather Nowcasting Technology].

Code Availability.—The official implementation of the AT loss is publicly available at <https://github.com/kaetsraeb/at-loss>.

* The author began this work at the Weather Radar Center and completed it at the AI/ML Innovation Research Center. bearsteak@cau.ac.kr

† hyeri.kim@ou.edu

‡ khkim777@korea.kr

§ Corresponding author: curseor@cau.ac.kr

- [1] M. Ghil and V. Lucarini, The physics of climate variability and climate change, *Rev. Mod. Phys.* **92**, 035002 (2020).
- [2] P. Stott, How climate change affects extreme weather events, *Science* **352**, 1517 (2016).
- [3] L. G. Cutillas-Lozano, M. S. C. López, A. P. Velasco, I. Andrés-Doménech, and J. Olcina-Cantos, Local-scale regionalisation of climate change effects on rainfall pattern: application to alicante city (spain), *Theoretical and Applied Climatology* **154**, 377 (2023).
- [4] H.-A. Kim, C.-H. Ho, J. Kim, E.-K. Seo, and S. K. Park, Observational study of a quasi-stationary mesoscale convective system during extreme rainfall on 8 august 2022 in korea, *Atmospheric Research* **325**, 108159 (2025).
- [5] D. Francis, R. Fonseca, N. Nelli, C. Cherif, Y. Yarragunta, G. Zittis, and A. Jan de Vries, From cause to consequence: examining the historic april 2024 rain-storm in the united arab emirates through the lens of climate change, *npj Climate and Atmospheric Science* **8**, 1 (2025).
- [6] J. T. Schaefer, The critical success index as an indicator of warning skill, *Weather and Forecasting* **5**, 570 (1990).
- [7] C. A. Doswell, R. Davies-Jones, and D. L. Keller, On summary measures of skill in rare event forecasting based on contingency tables, *Weather and Forecasting* **5**, 576 (1990).
- [8] M. Andrychowicz, L. Espeholt, D. Li, S. Merchant, A. Merose, F. Zyda, S. Agrawal, and N. Kalchbrenner, Deep learning for day forecasts from sparse observations (2023), [arXiv:2306.06079](https://arxiv.org/abs/2306.06079).
- [9] Y. Zhang, M. Long, K. Chen, L. Xing, R. Jin, M. I. Jordan, and J. Wang, Skilful nowcasting of extreme precipitation with nowcastnet, *Nature* **619**, 526 (2023).
- [10] J. Choi, Y. Kim, K.-H. Kim, S.-H. Jung, and I. Cho, Pct-cyclegan: Paired complementary temporal cycle-consistent adversarial networks for radar-based precipitation nowcasting, in *Proceedings of the 32nd ACM International Conference on Information and Knowledge Management* (2023) pp. 348–358.
- [11] G. Kochenberger, J.-K. Hao, F. Glover, M. Lewis, Z. Lü, H. Wang, and Y. Wang, The unconstrained binary quadratic programming problem: a survey, *Journal of Combinatorial Optimization* **28**, 58 (2014).
- [12] E. J. Gumbel, The return period of flood flows, *The Annals of Mathematical Statistics* **12**, 163 (1941).
- [13] X. Shi, Z. Chen, H. Wang, D.-Y. Yeung, W.-K. Wong, and W.-C. Woo, Convolutional lstm network: a machine learning approach for precipitation nowcasting, in *Proceedings of the 29th International Conference on Neural Information Processing Systems* (2015) pp. 802–810.
- [14] E. Costa, G. Scriva, R. Fazio, and S. Pilati, Deep-learning density functionals for gradient descent optimization, *Phys. Rev. E* **106**, 045309 (2022).
- [15] C. Klos and R.-M. Memmesheimer, Smooth exact gradient descent learning in spiking neural networks, *Phys. Rev. Lett.* **134**, 027301 (2025).
- [16] T. Albash and D. A. Lidar, Adiabatic quantum computation, *Rev. Mod. Phys.* **90**, 015002 (2018).
- [17] E. Farhi, J. Goldstone, and S. Gutmann, A quantum approximate optimization algorithm (2014), [arXiv:1411.4028](https://arxiv.org/abs/1411.4028).
- [18] Z. Wang, S. Hadfield, Z. Jiang, and E. G. Rieffel, Quantum approximate optimization algorithm for maxcut: A fermionic view, *Phys. Rev. A* **97**, 022304 (2018).
- [19] C. J. Maddison, D. Tarlow, and T. Minka, A* sampling, in *Proceedings of the 28th International Conference on Neural Information Processing Systems* (2014) pp. 3086–3094.
- [20] E. Jang, S. Gu, and B. Poole, Categorical reparameterization with gumbel-softmax, in *Proceedings of the 5th International Conference on Learning Representations* (2017).
- [21] J. Jo, A. Wagemakers, and V. Periwal, Annealing approach to root finding, *Phys. Rev. E* **110**, 025305 (2024).
- [22] C.-L. Tsai, K. Kim, H. Park, H. Park, W. Bang, and G. Lee, Association between upstream conditions and the intensity of orographic precipitation in the main mountain ranges of south korea, *Earth and Space Science* **12**, e2024EA003989 (2025).
- [23] X. Gao, H. An, W. Fang, X. Huang, H. Li, W. Zhong,

- and Y. Ding, Transmission of linear regression patterns between time series: From relationship in time series to complex networks, *Phys. Rev. E* **90**, 012818 (2014).
- [24] I. Ozken, D. Eroglu, T. Stemler, N. Marwan, G. B. Bagci, and J. Kurths, Transformation-cost time-series method for analyzing irregularly sampled data, *Phys. Rev. E* **91**, 062911 (2015).
- [25] A. M. Eskicioglu and P. S. Fisher, Image quality measures and their performance, *IEEE Transactions on Communications* **43**, 2959 (1995).
- [26] P. J. Huber, Robust estimation of a location parameter, *Ann. Math. Statist.* **35**, 73 (1964).
- [27] P. Charbonnier, L. Blanc-Feraud, G. Aubert, and M. Barlaud, Two deterministic half-quadratic regularization algorithms for computed imaging, in *Proceedings of the 1st International Conference on Image Processing* (1994) pp. 168–172.
- [28] W.-S. Lai, J.-B. Huang, N. Ahuja, and M.-H. Yang, Deep laplacian pyramid networks for fast and accurate super-resolution, in *Proceedings of the 30th IEEE Conference on Computer Vision and Pattern Recognition* (2017) pp. 5835–5843.
- [29] P. Nurmi, *Recommendations on the verification of local weather forecasts*, Tech. Rep. 430 (European Centre for Medium-Range Weather Forecasts, 2003).
- [30] P. Das, A. Posch, N. Barber, M. Hicks, K. Duffy, T. Vandal, D. Singh, K. v. Werkhoven, and A. R. Ganguly, Hybrid physics-ai outperforms numerical weather prediction for extreme precipitation nowcasting, *npj Climate and Atmospheric Science* **7**, 1 (2024).
- [31] J. W. Tukey, *Exploratory data analysis* (Addison-Wesley Publishing Company, 1977).
- [32] A. J. Sorby-Adams, J. Guo, P. Laso, J. E. Kirsch, J. Zabinska, A.-L. Garcia Guarniz, P. W. Schaefer, S. Payabvash, A. de Havenon, M. S. Rosen, K. N. Sheth, T. Gomez-Isla, J. E. Iglesias, and W. T. Kimberly, Portable, low-field magnetic resonance imaging for evaluation of alzheimer’s disease, *Nature Communications* **15**, 10488 (2024).
- [33] A. Zhao, A. Ermolaeva, E. Ullner, J. Kurths, S. Gordleeva, and A. Zaikin, Noise-induced artificial intelligence, *Phys. Rev. Res.* **4**, 043069 (2022).
- [34] Y. Dong, R. H. Chan, and S. Xu, A detection statistic for random-valued impulse noise, *IEEE Transactions on Image Processing* **16**, 1112 (2007).
- [35] A. Hore and D. Ziou, Image quality metrics: Psnr vs. ssim, in *Proceedings of the 20th International Conference on Pattern Recognition* (2010) pp. 2366–2369.
- [36] L.-C. Liu, C. Wu, W. Li, Y.-A. Chen, X.-P. Shao, F. Wilczek, F. Xu, Q. Zhang, and J.-W. Pan, Active optical intensity interferometry, *Phys. Rev. Lett.* **134**, 180201 (2025).
- [37] D. P. Kingma and J. L. Ba, Adam: A method for stochastic optimization, in *Proceedings of the 3rd International Conference on Learning Representations* (2015).
- [38] D. Ulyanov, A. Vedaldi, and V. Lempitsky, Improved texture networks: maximizing quality and diversity in feed-forward stylization and texture synthesis, in *Proceedings of the 30th IEEE Conference on Computer Vision and Pattern Recognition* (2017) pp. 4105–4113.
- [39] P. Ramachandran, B. Zoph, and Q. V. Le, Searching for activation functions (2017), arXiv:1710.05941.

END MATTER

Hyperparameter Settings.—In the experiments conducted with different objectives, the following common conditions were applied unless otherwise specified. Adam was used as the optimizer with momentum parameters $\beta_1 = 0.9$ and $\beta_2 = 0.999$ [37]. The batch size and learning rate were set to 16 and 0.0002, respectively. Instance normalization and the Swish activation function were incorporated into the hidden layers [38, 39]. The default threshold of 2 mm/h was applied for the AT loss and forecasting metrics. The value of the decaying τ in Eq. (5) was limited to a minimum of 0.05.

Additional Forecast Comparisons.—An additional case of 1-hour forecasts, issued at 17:10:00 UTC on June 5, 2024, is shown in Fig. 3. The AT loss produced the best forecasts from the 20-minute lead time onward, recording the highest CSI. In particular, it simulated the morphological changes of the precipitation echoes with substantial fidelity, outperforming the other baselines.

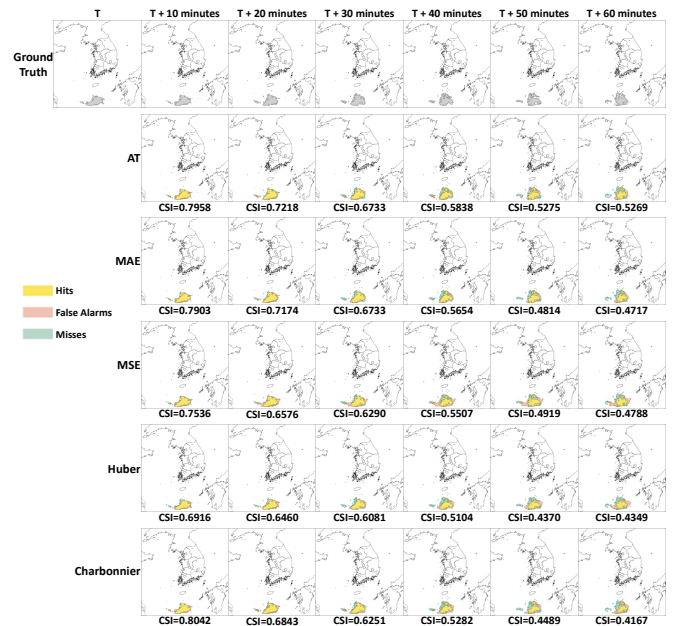


FIG. 3. A case of precipitation forecast comparisons from time T (2024-06-05 17:10:00 UTC).

CNN in Consistency Experiments.—To minimize the influence of model complexity, a minimal CNN architecture suitable for processing multi-dimensional data was adopted. This configuration, consisting of two convolutional layers with 16 and 1 feature maps respectively, used a kernel size, stride, and padding of 3, 1, and 1. The simplification of architectural factors enabled a more precise assessment of the performance of each loss function.